Sensors & Transducers, Vol. 274, Issue 3, October 2026, pp. 30-41

www.sensorsportal.com

Sensors & Transducers

Published by IFSA Publishing, S. L., 2026
http://www.sensorsportal.com

A Polarized Image Multiplexor for In-Line Frame Calculation in a Holographic Parallel Video Processor for 3D Dynamic Display

Branimir IVANOV, * Ginka IVANOVA and Deyan DIMOV
Institute of Optical Materials and Technologies, Laboratory 'Holography',
109, Acad. G. Bontchev Str., 1113 Sofia, Bulgaria
Tel.: + 33 617446640
E-mail: givanova@iomt.bas.bg

Received: 31 Aug. 2026 /Revised: 26 Oct. 2026 /Accepted: 29 Oct. 2026 /Published:30 Oct. 2026

Abstract: This article extends an existing eight-channel, non-polarized holographic optical trigger intended for real-time three-dimensional display by adding a polarizing beam-splitter layer. At each of the trigger's eight branches, a polarizing beam-splitter cube separates the arriving light into orthogonal S and P components, which two parallel encoder stages then address independently, doubling the trigger into 16 polarization-addressable channels. A fixed convention assigns the S- and P-branch channels to opposite depth-plane directions of a 49-plane display, with a polychromatic red–green–blue reference channel. The result is architectural economy: this construction reaches the same three-trigger-equivalent target achieved elsewhere with three physical triggers, using only two and doubling one of them through polarization cloning, the functional duplication of its branches, rather than physical duplication. The article also presents a layered numerical model of the recording medium, its recording energy budget, an optically recorded zoom transformation, and polarimetric measurements of the polarization states of a physically constructed trigger and its polarization-cloned counterpart. The emphasis throughout is methodological, prioritizing the cloning technique over further channel-count scaling.

Keywords: Polarization multiplexing, Holographic optical trigger, Volume holography, Polarizing beam-splitter cube, Silver-halide recording medium, Three-dimensional holographic display.

1. Introduction

Real-time three-dimensional holographic display places a substantial computational burden on any system that must generate a distinct wavefront for every depth plane, color channel, and frame of a moving scene. Digital computer-generated holography addresses this burden through dedicated processing hardware, algorithmic acceleration, or trained neural networks, and recent work has demonstrated real progress along each of these routes. One single-chip field-programmable gate array processor computes full-color, ultra-high-definition holograms in real time, expanding the viewing angle through a dedicated steering-backlight unit, not through the native pixel count of the spatial light modulator (SLM) alone [1]. A single-step Fresnel calculation based on the split-Lohmann method computes an entire multi-depth scene in constant time regardless of the number of depth planes represented; conventional layer-based computation does not share this property, since its calculation time grows in direct proportion to depth-layer count [2]. Even so, both results depend on continuous, per-frame computation that dedicated processing hardware carries out for as long as the display operates. The display's space–bandwidth product imposes a direct trade-off between image size and viewing angle: with a fixed pixel count, increasing one necessarily decreases the other [1]. A recorded or multiplexed holographic

medium is not constrained in the same way, since the structure of the recording medium itself, rather than a discrete, fixed pixel array, sets its spatial resolution [3].

The present work continues a line of research into an all-optical holographic video graphics processing unit, referred to throughout as the HVGPU, in which channel and depth-plane multiplication are properties of the recording and of a small number of passive optical elements, established once during fabrication rather than recomputed for every frame [4, 5].

In-line frame calculation in the title refers to this multiplication of each input frame into depth-plane frames while the frame passes through the trigger, and not to a measured calculation speed.

1.1. Multiplexing as a General Principle in Holography

Multiplying the number of independently addressable channels obtainable from a single optical element, by exploiting some physical property of the illuminating light rather than by duplicating hardware, is an established and currently active strategy across several branches of optics. Two general routes toward that end are considered below: polarization specifically, since it forms the basis of the present architecture, and other physical degrees of freedom pursued for the same purpose elsewhere in the literature.

Polarization has itself been the subject of formal multiplexing frameworks in holography. A recently proposed orthogonal matrix of polarization combinations enables four or more independently addressable holographic channels recorded at a single position within a polarization-sensitive material, selectively reconstructed according to the polarization combination of the illuminating reference wave [6]. This particular doubling mechanism has already been explored in our earlier work: an infrared holographic optical element reported over a decade earlier used the same principle at smaller scale, separating two wavelength channels into four by their S- and P-polarized components [7]. Nor is orthogonal polarization multiplexing confined to linear states; a recent all-dielectric metasurface superimposes two independent holographic phase patterns addressed by orthogonal circular polarization, generating different structured-light outputs depending on whether the illumination is right- or left-circularly polarized, with an extension to spatially multiplexed channels at independently controlled focal planes [8]. Polarizing beam-splitter cubes performing a similar selective folding also appear in current commercial-grade near-eye optics, relaying holographic content through a compact eyepiece path [9]. Polarization can also change dynamically rather than remaining fixed at fabrication: fast-response liquid-crystal phase shifters, paired with polarization gratings, steer a single SLM's holographic output between several discrete positions in rapid temporal sequence, exploiting human visual persistence to create the impression of an enlarged display area [10].

More elaborate schemes push polarization multiplexing further still. Because the number of independently addressable polarization channels achievable from a single metasurface layer is fundamentally limited by the degrees of freedom of the Jones matrix – a ceiling of three channels under conventional orthogonal-polarization design [11, 12] – recent work has turned to deliberately engineered noise in the metasurface response to exceed that limit, reaching 55 distinguishable channels when combined with an additional axial focal-plane offset and neural-network optimization [11]. Researchers have since extended the same noise-engineered approach to combine polarization with position, wavelength, and orbital angular momentum, individually and simultaneously, within a single device, each additional physical degree of freedom multiplying the addressable channel count further [12]. The present architecture applies polarization as an orthogonal, physically realizable selecting variable through a dedicated polarizing beam-splitter-cube layer added ahead of an existing non-polarized channel set, rather than through engineered metasurface response.

1.2. Other Physical Degrees of Freedom Used for Holographic Multiplexing

Polarization is one instance of a broader family of techniques that recover multiple independent optical functions from a single element by varying some controllable property of the illuminating beam. Orbital angular momentum offers another such property. Recent work encodes independent image channels into distinct orbital-angular-momentum modes for large-field-of-view multiview display [13]. A further extension introduces a synthetic, mathematically defined operator dimension beyond orbital angular momentum's own physical mode index, addressing a broader constraint: the intrinsic physical degrees of freedom conventionally exploited for holographic multiplexing were approaching the limits of further scaling. Subdividing a single orbital-angular-momentum channel by an engineered coordinate-transformation operator yielded a ninefold capacity increase over conventional orbital-angular-momentum holography [14].

Angle of incidence under Bragg selectivity is a third such property: a multiplexed holographic optical element can hold two entirely different optical functions in superposition; the angle of a variable-focus illumination lens, rather than polarization, selects between them [15]. Beyond these, researchers have developed a wider taxonomy of multiplexing techniques – including shift, peristrophic, phase-coded, and correlation-based schemes – principally for holographic data storage rather than display; the present article does not develop these further [16].

1.3. Scope and Relation to Prior Work

An earlier study [4] describes and characterizes the eight-channel, non-polarized beam-splitter unit that anchors the present architecture: a splitter delivering eight physical output branches, a downstream encoder of half-wave plate rotators, and a beam combiner, with each branch carrying a distinct linear polarization angle generated from a single input beam. The present article, a continuation of the OPAL' 2026 design and fabrication study [5], takes that unit as a fixed starting point and does not re-derive or re-characterize it.

Relative to our previously reported eight-branch holographic trigger [4, 5], the present work introduces one specific architectural extension: each of the eight inherited branches is separated into orthogonal S and P components by a dedicated polarizing beam-splitter cube and processed by two parallel encoder stages, which produces 16 simultaneously accessible polarization-resolved optical paths from the original eight (Section 3). The contribution introduced in this study is therefore the polarization-branch duplication architecture based on the polarizing beam-splitter and its experimental characterization, and not the underlying eight-channel trigger, polarization multiplexing in general, or the previously reported 49-plane display concept. The separation into S and P components was already applied to a two-wavelength input in an earlier four-channel element [7]. The extension beyond the prior OPAL' 2026 conference publications [4, 5] consists of two new experimental results: the exposure dependence of the diffraction efficiency of the three U04 color holograms (Section 5) and the polarimetric measurements of the polarization states of the physical and polarization-cloned branches (Section 6). It also includes three design results: the architecture and channel accounting presented in Section 3, the recorded zoom transformation described in Section 4, and the layered numerical model with the recording energy budget presented in Section 5. The treatment of the recording material is limited to those properties required to interpret these results.

2. Theoretical Background

2.1. Volume Holography and Bragg Selectivity

A hologram is classified as thin or as thick (volume) according to whether the reconstruction beam interacts with a single recorded interference plane or with many recorded planes distributed through the thickness of the recording layer. The Klein–Cook parameter formalizes this distinction:

$$Q = 2\pi\lambda_0 d/(n_0\Lambda^2), \quad (1)$$

where λ_0 is the illumination wavelength in air, d is the recording-layer thickness, n_0 is the medium's average refractive index, and Λ is the interference-fringe period. Values of Q greater than unity place a grating in the volume, or Bragg-diffracting, regime, requiring a coupled-wave rather than a simple grating-diffraction analysis [16]. In this regime, Kogelnik's coupled-wave theory governs reconstruction, relating diffraction efficiency to the recording layer's thickness and its induced refractive-index or absorption modulation. This theory remains the standard theoretical treatment of thick-hologram diffraction efficiency across the volume-holography literature [17]. The recording medium used in the present work, described in Section 5, operates in this volume regime.

Depth distortion in a thick hologram does not occur when the geometry of the illumination beam at reconstruction exactly matches the geometry of the reference beam used at recording; this geometric correspondence is the governing condition for distortion-free reconstruction [17]. Distortion specifically arises when the reconstruction illumination is not aligned with the optical axis of the original reference beam; when that alignment is exact, no such distortion occurs. This criterion underlies the zoom transformation described in Section 4, achieved by varying the convergence or divergence angle of the illuminating beam rather than by digitally resampling an already-encoded pattern.

2.2. Wavefront Cloning

A hologram that records the wavefront produced by a physical optical element, whether a lens, a prism, or a more complex objective, reproduces the transformation that element applies to the illuminating wave, within the angular and spectral selectivity of the recording, for a subsequent wave passing through the recorded copy [18, 19]. At reconstruction in the recording geometry, the reconstructed wavefront approximates the wavefront that the original element would have produced, within the angular and spectral selectivity and the resolution of the recording. It follows that a SLM, displaying a computed interference pattern rather than a fixed recorded one, can synthesize the equivalent of a physical optical element without that element existing in bulk form. Switching the displayed pattern between frames is, by the same logic, functionally equivalent to physically exchanging optical elements at frame rate.

Both analog and digital contexts demonstrate this same principle: an interference pattern, whether recorded on a fixed medium or generated dynamically by a SLM, can carry an intended optical transformation while preserving the phase information of the reconstructed wavefront. Recent digital work, for instance, encodes a comparable rescaling transformation directly into a computed hologram's phase structure while explicitly tracking its effect on reconstruction depth [20].

The zoom transformation described in Section 4 applies the same underlying principle by physical

rather than computational means. The recording medium described in Section 5 records a real optical system's convergence and divergence behavior as an interference pattern, so that reconstructing that recorded pattern provides the convergence and divergence behavior of the zoom optics, for the recorded geometry, without requiring them to remain part of the operating system.

As in elemental-image-array approaches to light-field imaging, many elementary recordings construct a multichannel hologram of the kind described in Section 3, each differing from the others by its parallax angle relative to the recorded object; each elementary hologram, in effect, views the object from its own distinct angle [21].

3. Architecture of the Polarized HVGPU

3.1. Inherited Non-Polarized Splitter Architecture

The present architecture takes as its starting point a non-polarized, eight-channel beam-splitter unit and its associated encoder and combiner stages, described in full in our previous papers [4, 5]. The present article requires only two properties from that inherited architecture. The splitter delivers eight physical output branches from a single input, preserving the input beam's phase, polarization, and wavelength unaltered across all eight branches.

A downstream encoder stage then assigns each branch a distinct, though not necessarily orthogonal, linear polarization angle by setting a half-wave plate so that the polarization angle takes one of eight values from 0° to 70° in 10° steps. A half-wave plate whose fast axis is at an angle α to the input polarization rotates linear polarization by 2α, so these settings correspond to plate orientations from 0° to 35° in 5° steps.

In this base architecture, angle rather than orthogonality separates adjacent channels; two states are distinct as long as they differ, whether or not they are perpendicular to one another. The addition described in the remainder of this section builds on that base without altering it and treats the base splitter and its eight branches as a given configuration.

Throughout, a branch is one of the eight outputs of the splitter; a channel is one physical optical path through the trigger, so that each branch gives an S channel and a P channel; a color component is one wavelength carried by a channel; a virtual color channel is one color component in one channel; a depth plane is one image plane of the display; and a trigger is the complete multichannel device.

3.2. The Polarizing Beam-Splitter Layer

A polarizing beam-splitter cube is introduced ahead of the encoder stage at each of the eight branches produced by the inherited splitter. Each cube divides the light arriving at its branch into two orthogonally polarized components, S and P, which propagate onward as two physically separate beams. Applied across all eight branches, this yields 16 output beams: eight carrying the S-polarized component of their respective branch (S_1 through S_8) and eight carrying the P-polarized component (P_1 through P_8). S and P are, by construction, mutually orthogonal. This orthogonality is a stronger property than the mere distinctness the inherited eight-channel angle encoding relies upon, and the present architecture applies it deliberately, as an additional, independent multiplication of the channel count rather than as a replacement for the angle-based distinctness already present in the inherited base. S and P are not the only pair of states with this property; any pair of mutually orthogonal polarization states could in principle serve the same role, circular polarization included, but S and P are the simplest and most directly obtainable pair from a single passive cube.

Of the two orthogonal outputs at each branch, we arbitrarily designate one to continue propagating in the same direction as the branch's original beam – here, the S-polarized output. The P-polarized output, newly generated by the cube, travels onward to a second, physically separate encoder stage.

In this article, “polarization cloning” is an engineering term for the functional duplication of a processing branch: the cube decomposes the light of each branch into orthogonal S and P components, and each component is processed by its own encoder, so that the P branch carries the same eight channels of image information as the S branch in the orthogonal polarization state, which is the sense in which it performs the function of a second, separately built trigger. No claim of equal diffraction efficiency or power is made. The term does not refer to quantum cloning or to cloning of an arbitrary polarization state, which a passive polarizing beam-splitter cube does not perform.

3.3. Dual Encoder Architecture: S-Branch and P-Branch

Two encoder stages operating in parallel process the 16 channels the polarizing beam-splitter layer produces, each stage a direct copy of the encoder already established in the inherited base architecture, each built from eight half-wave plates. The first encoder receives the eight S-polarized channels and applies the base architecture’s own angle assignment unmodified: polarization angles from 0° to 70° in 10° steps, one angle per channel. The second encoder receives the eight P-polarized channels and otherwise matches the first exactly; only its polarization angles differ, offset by exactly 90°; its plates are mounted at the S-branch orientations plus 90°. This offset reflects the 90° separation between S and P at the point where the two branches diverge; the second encoder is

otherwise an unmodified reproduction of the first rather than an independently designed unit.

The encoder stage performs continuous checks on the calculated polarization angle assigned to each channel during operation. Polarization angles are normalized modulo 180°, since orientations of linear polarization that differ by 180° describe the same polarization axis, and duplicate orientations are rejected to preserve channel distinguishability. The encoder checks and corrects this condition during operation, in the same manner the base architecture's own angle-assignment function already requires; extending this checking to 16 channels across two encoders, rather than eight channels across one, adds negligible additional computational burden.

3.4. Mapping Polarization Branches to Depth Planes

A fixed convention assigns the 16 channels the S- and P-branch encoders produce to the display's depth planes. The eight S-branch channels, S_1 through S_8, go to the 24 depth planes on one side of the reference plane (8 × 3 colors), and the eight P-branch channels, P_1 through P_8, go to the 24 depth planes on the other, each channel carrying all three color components.

This mapping is a deliberate representational choice adopted for clarity of exposition, not a physical necessity imposed by the polarization mechanism itself; S and P carry no inherent association with depth sign, and the assignment could in principle be made differently. The convention is nonetheless useful, since it gives the architecture's two most naturally distinguished quantities, the sign of depth displacement and the S/P polarization axis, a single, consistent correspondence throughout the remainder of this article.

Fig. 1 summarizes this dual-branch architecture. The inherited splitter's eight outputs each feed a polarizing beam-splitter cube, producing the S- and P-polarized branches described above. The eight channels in each branch pass through their respective half-wave plate sets and encoders – identical in structure, offset by 90° in angle between the two – before recombining through eight-input beam combiners at the combiner stage, reproducing the base architecture's splitter-to-combiner path twice over rather than once.

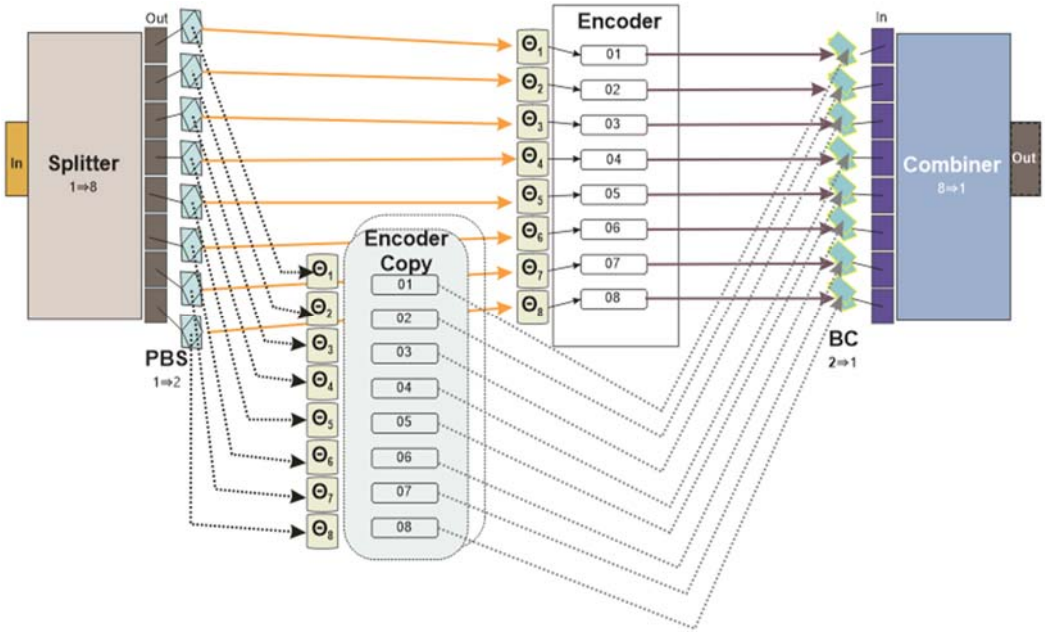


Fig. 1. Polarized HVGPU architecture: an eight-channel splitter (1→8) feeds eight polarizing beam-splitter cubes PBS (1→2), each separating its branch into orthogonal S and P components. The physical encoder and its copy – with the polarization angles Θ_1–Θ_8 set by the half-wave plates and transformation functions 01–08 in each – process the S and P branches independently before both branches recombine through a beam combiner BC (2→1) and enter the eight-input channels of the combiner unit (8→1).

3.5. On-Axis Propagation

At every channel, the image propagates along the optical axis rather than off-axis. This choice avoids the need for compensation of the geometric distortions that off-axis propagation would otherwise introduce, and follows directly from the reconstruction-geometry criterion given in Section 2.1: keeping both recording and reconstruction beam geometry on the optical axis most straightforwardly maintains their exact correspondence. This article makes no claim regarding the relative merits of off-axis architectures generally; it describes and characterizes the on-axis

configuration actually built, and leaves treatment of off-axis alternatives to future work.

3.6. The Reference Channel and Whole-Assembly Positioning

A 49th channel, sourced from a single physical output of a separate, ordinary eight-channel non-polarized trigger, serves as the reference plane against which the 24 positive and 24 negative depth planes are measured. Like each of the 16 polarization-derived channels, the reference channel carries the red, green, and blue components. The three components co-propagate spatially in the reference channel and remain spectrally distinct, together forming a polychromatic RGB reference beam. No component appears at an intermediate wavelength: a spectrometer in this channel records three lines at 632.8, 532, and 488 nm, and a detector or the eye receives the sum of the three intensities, which is perceived as a mixed color by additive mixing. These components all carry the unmodified reference image, so they share one channel number and constitute a single reference plane. Counted by color, they are three virtual color channels. The reference channel is controlled in the same manner as the other 48 channels, rather than treating it only as a passive positional marker.

Because the physical spacing between the reference channel and each of the 48 depth-plane channels is fixed by construction, a single translation applied to the reference channel alone repositions the entire 49-plane assembly along the propagation axis as a rigid whole. The assembly's overall standoff distance from the source thereby becomes one adjustable quantity, governed at the reference channel, rather than 48 separately tracked positions across both branches of the polarization-cloned trigger.

3.7. Physical-to-Virtual Channel Accounting

The architecture described above amounts to an equivalence, presented here in those terms: a single physical trigger, augmented with the polarizing beam-splitter layer described in Section 3.2, is designed to reproduce the function of two separately constructed physical triggers. Building the 16-channel polarized trigger described here, together with the single reference channel drawn from a separate ordinary trigger, therefore reaches the same three-trigger-equivalent target architecture as an all-non-polarized, three-physical-trigger implementation, using two physical triggers rather than three. This article offers it as a description of the method's structural economy – reaching a given target architecture by a different, more economical route – rather than as an argument for the value of channel-count scaling as such.

The economy is one of hardware and not of optical power: the polarizing beam-splitter cube divides the power of each branch between its S and P outputs, so that, for an ideal lossless cube, each of the 16 polarization-separated channels receives half of the power of the corresponding channel of a non-polarized trigger illuminated by its own full beam. This halving is the price of saving the second trigger; it can be recovered through the source power and, in recording, through exposure (Section 5.3), and a complete power budget is not characterized in this article.

The present article's emphasis is on the polarization technique itself, and on the design of a polarization-cloned trigger intended to reproduce the function of a physically constructed one, not on the raw number of channels obtainable by extending the technique further.

In total, the architecture described in this section comprises 17 active physical channels: the 16 polarization-separated channels that the polarizing beam-splitter layer produces from the eight paths of the inherited splitter (eight S and eight P), plus one reference path taken from a single output of a separate, ordinary eight-channel non-polarized trigger, with the other seven outputs left unused. Each of the 16 polarization-separated channels carries the red, green, and blue components, giving $16 \times 3 = 48$ virtual color channels, 24 in each branch. Together with the single reference plane, this realizes 49 depth planes; counted by color, the reference path carries three components, so the total is 51 virtual color channels.

4. Optical Implementation and Recorded Realization of a Function

Eliminating translating bulk optics from a zoom function is a design goal pursued across imaging systems generally, independent of any holographic context. Deformable-mirror-based zoom systems, for example, achieve variable focal length by reshaping a mirror surface under microactuator control, avoiding lens-group translation altogether; such systems report zoom ratios on the order of 2×, with each new target focal length requiring fresh calculation of the required surface profile and per-actuator voltage control to manage the aberrations the reshaped surface itself introduces [22]. The present work shares the goal of a zoom function without translating bulk elements, but pursues it by a different route.

In the encoder stage described in Section 3.3, between the half-wave plate rotators and the combiner, an optical teletransfer system gives each channel independently controllable beam convergence or divergence. This sets the effective distance of the channel's reconstructed depth plane by the mechanism of Section 2.1: varying the convergence or divergence angle of the illuminating beam relative to the geometry used at recording. The axis of the illuminating beam stays coincident with that of the recording reference beam, so the reconstruction remains free of depth distortion. Here the optical function of this zoom teletransfer system is recorded as an interference

pattern directly in the recording medium of Section 5, forming a thick hologram of the teletransfer optics and not a digitally computed or resampled pattern.

Reconstructing this recorded pattern provides the convergence and divergence behavior of the teletransfer system for the recorded geometry, by the wavefront-cloning principle of Section 2.2, so that the physical zoom optics need not remain part of the operating system.

A digital reproduction of the same function with a spatial light modulator, for instance a computed phase pattern equivalent to a variable-focal-length Fresnel lens, is a natural extension of this principle. Such a realization would make the zoom state reconfigurable, in contrast to the fixed recorded pattern of the present implementation, and is left for future work.

5. Recording Medium and Energy Budget

5.1. Recording Medium

The present work employs U04 silver-halide holographic emulsion as the recording medium, in accordance with the original architecture [4]. U04 is an iso-panchromatic silver-halide emulsion with a 4 nm average grain size, a resolution of 18000 lines/mm, and spectral sensitivity spanning 440-700 nm, sufficient for recording all common holographic laser wavelengths without diffusion-related blur [23]. Whereas the design and fabrication study [5] used the LiMo silver-halide formulation, the present work returns to U04.

Each holographic plate consists of a photosensitive layer approximately 4 μm thick, deposited over an underlayer approximately 0.4 μm thick, both supported on a glass substrate. For monochrome recording of a reflective diffuse object, [23] reports a diffraction efficiency of 98 % for this medium. This article limits its materials treatment to the properties needed to interpret the layered model and energy budget below, and does not attempt a comprehensive characterization of U04. It makes no systematic comparison between recording emulsions, since the aim is to characterize what the present technique achieves with this medium.

5.2. Layered Numerical Model of the Recording Medium

Rather than treat the active layer of U04 as a single, uniformly responding medium, this article models it as a stack of thin slices, each acting as a thin diffraction grating, which must operate in phase with one another for the reconstructed image to build correctly. This is a numerical discretization only: a layer of about 4 μm sampled at a nominal spatial step of 4 nm, the grain size reported for U04 [23], contains about 1000 slices, which should not be interpreted as 1000 physically distinct diffraction gratings. The recorded grating period is determined by the interference geometry and the wavelength and not by the grain size; for a reflection recording at 532 nm in a medium of refractive index near 1.5, the fringe planes are about 177 nm apart, which gives of the order of 20 Bragg planes across the layer.

5.3. Recording Energy Budget

In the present work, ordinary exposure-energy management – rather than any active optical gain mechanism – recovers the diffraction efficiency lost to the additional absorption that the added polarizing-beam-splitter layer and its associated second encoder introduce. Recording quality depends on matching the object-beam and reference-beam intensities for maximum interference contrast, and extending exposure time for a given channel, within the linear part of the recording material's exposure characteristic, compensates for any reduction in available signal at that channel (Fig. 2).

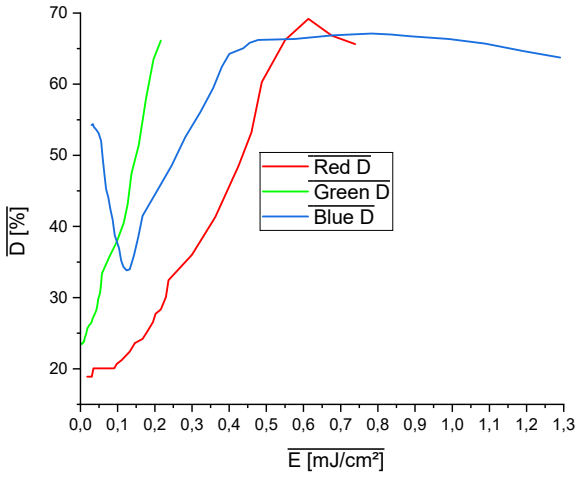


Fig. 2. Dynamic Range of the R–G–B Diffraction-Efficiency Response in the U04 Emulsion.

The developers of the emulsion recommend a minimum exposure of 320 μJ/cm² per color component for full-color recording, rising to roughly 600 μJ/cm² for monochrome [23]. In this work, exposures ranging from 320 μJ/cm² up to 1.2 mJ/cm² were investigated.

In the present measurements (Fig. 2), the maximum diffraction efficiencies of the U04 plates are about 69 % in the red, 66 % in the green, and 67 % in the blue, reached at exposures of about 0.6, 0.2, and 0.8 mJ/cm², respectively. For comparison, [24] reports values above 50 % for an emulsion with a 10 nm grain under different exposure conditions, and [23] reports 98 % for monochrome recording of a reflective diffuse object. For a color holographic optical element such as the HVGPU, however, the quantity that matters is not the maximum efficiency of each color but the balance

among the three, since the relative output powers of the red, green, and blue components determine the white balance perceived by the eye. This balance is reached at operating efficiencies well below the maximum attainable for one or two of the colors, and it is set by the exposure of each color hologram and by the source powers. The lower maxima of the present plates, which we attribute to a recording and swelling procedure not optimized for peak efficiency, therefore do not by themselves impair the operation of the element.

The efficiency cost of recording several wavelengths together in one shared layer, instead of in separate per-color recordings as here, has been measured elsewhere: a photopolymer volume hologram recorded with red, green, and blue exposed together reached per-channel diffraction efficiencies of 34 % to 67 % (mean 53 %), the shortest-wavelength channel receiving the least favorable exposure in that configuration [3]. This is consistent with our choice of a separate recording medium per color, which allows independent control of exposure and phase for each color component.

6. Experimental Characterization

The following measurements characterize the individual color holograms comprising the present architecture, and the polarization states of the physical and cloned branches of the trigger. We obtained the diffraction-efficiency values reported in Fig. 2 following the exposure procedure described in Section 5. We characterized each of the three color components – recorded independently at 632.8 nm, 532 nm, and 488 nm on separate U04 plates – individually before assembly into the S/P-cloned trigger, to obtain a per-color baseline against which we could later judge the combined trigger's behavior.

6.1. Polarization-State Verification

The polarization states at the output of the optical processor were verified with a polarimeter placed at its end, that is, after the beam-splitter unit, the encoder unit, and the beam-combiner unit, so that each measurement includes the combined effect of all three units. The polarimeter is a Thorlabs PAX1000VIS/M, which operates in the visible spectral range and was set to the wavelength of each color component (632.8, 532, and 488 nm).

The measurements confirm that the assembled processor – the splitter units that form the S and P branches (Section 3.2), followed by their encoder units (Section 3.3) – produces the intended polarization angles and not only the nominal design values. Fig. 3 presents the results for the three color components – red (Fig. 3a), green (Fig. 3b), and blue (Fig. 3c) – sampled at representative polarization angles from the full 16-channel set: 0°, 20°, and 70° for the physical S-branch trigger, and 90° and 160° for the polarization-cloned P-branch trigger.

Each panel shows the measured polarization ellipse together with its azimuth and ellipticity angle; an ellipticity angle of 0° corresponds to ideal linear polarization. The polarimeter reports azimuths in the interval from −90° to +90°, so the readouts of about −20° in the 160° panels are equivalent to 160° modulo 180°, in agreement with the periodicity of linear polarization (Section 3.3).

The azimuths printed in the panels agree with the nominal polarization angles within 0.7° in 13 of the 15 measurements and within 2.4° in the remaining two (red at 70° and 160°), and the ellipticity angles are at most 3.8°, so all measured states are close to linear. An ellipticity angle of 3.8° corresponds to a minor-to-major axis ratio of 0.07 in amplitude, that is, an orthogonal component of about 0.4 % of the intensity. The largest azimuth deviation, 2.4°, is less than half of the 10° spacing between adjacent channels, so each measured state remains closer to its own nominal angle than to that of a neighboring channel.

The polarization-cloned P branch reproduces the polarization quality of the physical S branch: its largest azimuth and ellipticity deviations are 1.8° and 3.2°, against 2.4° and 3.8° for the S branch. The panel labels are the azimuths of the linear polarization read on the polarimeter, referred to the polarization axis of the S branch at the encoder input, and not mechanical positions of the half-wave plate axes.

A plate whose fast axis is at an angle α from this axis maps a linear polarization at an angle ψ to $2\alpha - \psi$. The S-branch plates receive $\psi = 0°$ and, at α from 0° to 35°, produce 0° to 70°. The P-branch plates receive the orthogonal polarization $\psi = 90°$ and are mounted at the S-branch orientations plus 90°, so that they produce 90° to 160°.

Crosstalk between adjacent channels is not evaluated here, since no pair of successive channels was measured in this article; it is reserved for the companion paper on the base architecture.

6.2. Scope of the Comparison between the Physical and the Cloned Trigger

The polarization states of the physical S-branch and the polarization-cloned P-branch are compared in Fig. 3, and the per-color diffraction-efficiency baselines of Fig. 2 were measured before assembly. A direct comparison of the diffraction efficiencies of the physical and the cloned trigger, with uncertainties, is not carried out in this article and is reserved for a subsequent publication.

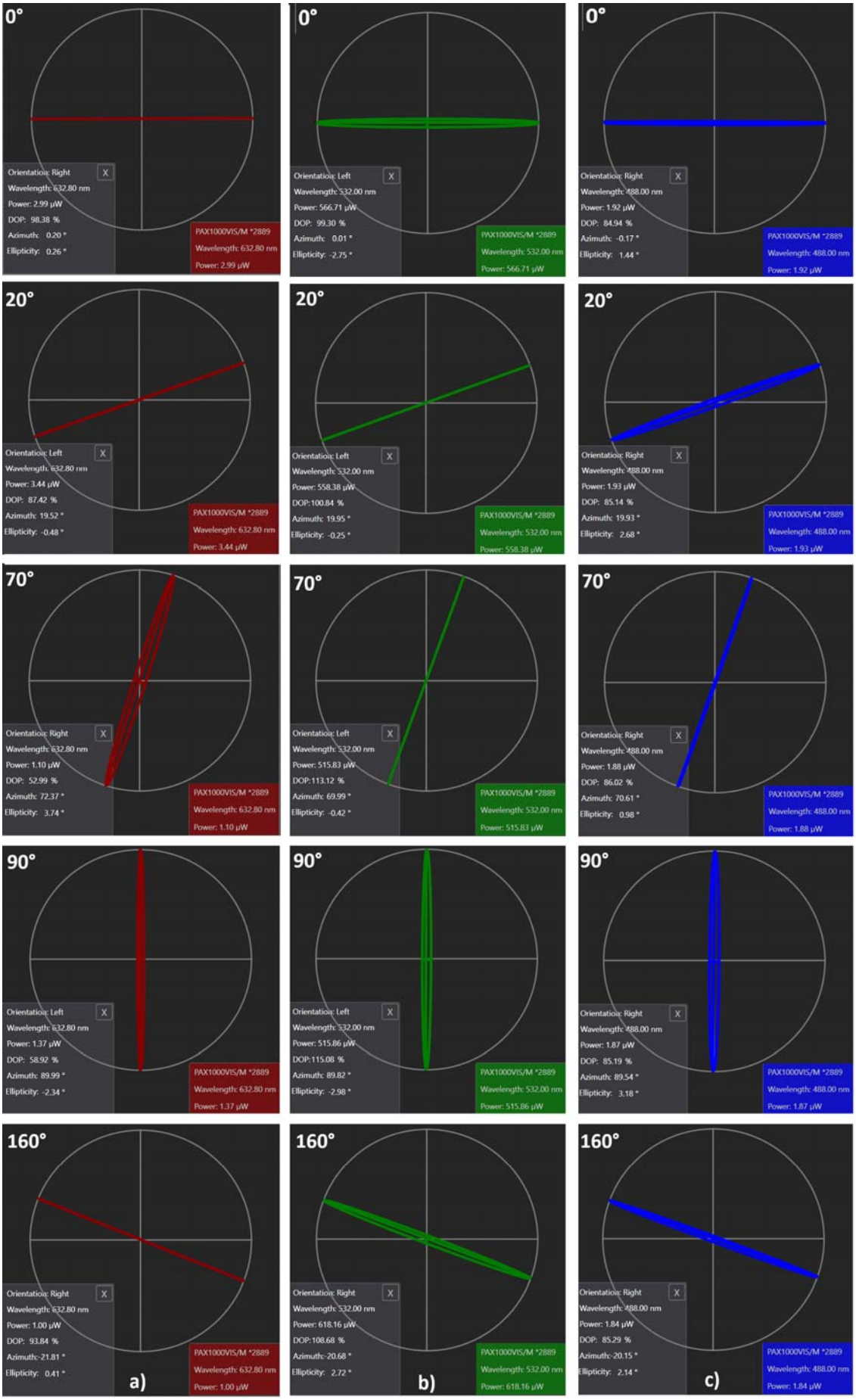


Fig. 3. Polarization azimuths of physical trigger (0°, 20°, and 70°) and polarization-cloned trigger (90° and 160°).

7. Discussion

7.1. Efficiency and Crosstalk across Polarization-Multiplexing Mechanisms

The efficiency cost of polarization-based multiplexing depends strongly on the physical mechanism performing the channel separation. Where multiple holograms are recorded as overlapping interference patterns at a single position in an anisotropic material and distinguished at readout by reference-wave polarization, diffraction efficiency falls to a fraction of a percent as channel count increases, even as crosstalk remains low: approximately 6×10^{-4} for a four-channel polarization-holographic recording in a photoinduced-anisotropic material [6]. Metasurface-based approaches that engineer a departure from strict polarization orthogonality to exceed the three-channel Jones-matrix limit report substantially higher per-channel efficiencies: 19 % to 28 % for polarization multiplexing alone, and 10 % to 16 % when combining polarization with wavelength multiplexing across 10 channels. Both approaches confirm that crosstalk grows as channel count increases, and at least one configuration requires active optimization to correct uneven energy distribution among channels [11, 12]. Researchers have measured polarization-based folding of the optical path in near-eye relay optics – built from cascaded quarter-wave plates, polarizing beam-splitters, and half-mirrors – at 8.5 % to 17.5 % against a 25 % theoretical maximum. They attribute the shortfall to imperfect polarization states and component performance rather than to any flaw in the underlying principle [9]. Where polarization switches dynamically in time rather than remaining fixed at fabrication, researchers have measured cascaded liquid-crystal phase-shifter stages at approximately 80 % transmittance per stage, with total transmission falling approximately as 0.8 raised to the number of cascaded stages [10]. The present architecture separates its 16 channels spatially, at a single polarizing-beam-splitter layer positioned once ahead of the encoder stage, rather than through repeated cascaded stages, overlapping recordings at one location, or engineered departure from polarization orthogonality; Fig. 2 reports its own measured diffraction efficiency.

7.2. Parameter Sensitivity: Robustness versus Security

Design priorities for polarization-based multiplexing depend heavily on the intended application. Display designers typically treat extreme sensitivity to small parameter deviations as a limitation to engineer around; elsewhere, researchers have deliberately exploited comparable sensitivity as a security feature instead. One holographic encoding scheme requires exact alignment of several interdependent optical parameters for correct reconstruction, with a propagation-distance error of only 0.1 cm sufficient to destroy the reconstructed image entirely [14]. The present architecture pursues the opposite goal, favoring robust, stable channel separation from a small number of fixed, passive optical elements over fine parameter sensitivity in either direction.

Polarization can also select between distinct behaviors of a single fixed element: a nonlinear flat-optics edge detector reconstructs edges in different directions depending on the polarization of its illumination [25]. This differs from the channel multiplication described here, but it relies on the same underlying principle: a controllable property of the illuminating beam governs the behavior of a fixed passive element.

7.3. Active versus Passive Channel Generation

Polarization can also switch dynamically in time, instead of being fixed at fabrication. Fast-response liquid-crystal phase shifters paired with polarization gratings steer the output of a single SLM between discrete positions in rapid sequence, synchronized frame-for-frame with the refresh rate, so that viewers perceive positions occupied one at a time as simultaneous, through persistence of vision. The same work reports that the perceived brightness per position falls in proportion to the number of positions, because a fixed instantaneous optical power is divided across sequential time slots and not distributed once across permanently separate paths [10]. The present architecture divides the power spatially, once, at the polarizing-beam-splitter layer: its 16 channels exist simultaneously as separate polarization-resolved paths, without time multiplexing, so that no switching speed or synchronization is required to separate them. The two approaches serve different goals: enlarging the effective projection area of a single SLM in one case, multiplying the channel count of one recorded trigger in the other.

7.4. Digital Computational Alternatives for Multi-Depth Reconstruction

Real-time, full-color holographic video by digital means is possible, though at a substantial engineering cost. A slim-panel holographic video display computes full-color, ultra-high-definition holograms at 30 frames per second with a custom single-chip processor built for the task, and expands the viewing angle about 30-fold through a dedicated steering-backlight unit [1]. Not every digital approach scales poorly with the number of depth planes: a single-step Fresnel calculation based on the split-Lohmann method computes a multi-depth scene in constant time regardless of depth-layer count, up to

18 times faster than conventional layer-based computation, but it still depends on dedicated graphics-processing-unit hardware computing a fresh hologram every frame and has its own constraints, a minimum reconstructible depth and a residual lateral-shift artifact [2]. Other digital approaches to related multi-depth or multi-view problems report substantial training overhead, tens of hours of network training in more than one case [26], and typically represent scenes by a small number of discrete depth or view states, a number set mainly by computational cost: three depth planes in one recent multi-depth holographic display [9] and eight accommodation states in a near-eye light-field reconstruction system [26].

The distinction between these digital results and the present architecture is not that digital multi-depth computation cannot be made fast or cannot scale; recent results show that it can be made both. The distinction is that digital computation, however fast, must run continuously, once per frame, for as long as the display operates, whereas channel and depth-plane multiplication in the present architecture is a fixed property of the recording and of the polarizing-optics layer, established once during fabrication rather than recomputed indefinitely. The throughput of the present architecture is therefore bounded by the refresh rate of the source of the input frames, a HOLOEYE LETO-3-VIS-009 phase-only spatial light modulator [27], whose manufacturer-specified input frame rate is 60 Hz, or 180 Hz in color-field-sequential mode. In our setup it projects 90 monochrome frames per second, which corresponds to 4410 depth-plane sub-frames per second for 49 planes, as in the base architecture [4]. Source modulation, synchronization, detector response, scene updating, and end-to-end latency are not characterized in this article. This reflects a broader motivation shared with unrelated recent work in other areas of optics entirely: researchers have proposed all-optical analog computing as a remedy for the complexity, power consumption, and speed limitations inherent to digital signal processing generally [25].

7.5. Design Perimeter: Technique over Channel Count

The central claim of the present article is methodological rather than a claim about achievable scale. A polarization-cloned trigger, generated from a single physical trigger by the polarizing-beam-splitter layer described in Section 3, provides orthogonally polarized copies of the eight branches, and the measured polarization states of the physical and cloned branches (Fig. 3) are consistent with this design. Whether the cloned trigger matches an independently constructed one in diffraction efficiency remains to be shown.

Three further routes to multiplying channel count are noted as directions available to the present technique, rather than as content developed or characterized here. These are: additional physical degrees of freedom, such as a further polarizing-prism type beyond the polarizing beam-splitter cube used here (a Wollaston or Glan prism); further zoom-state, global-convergence, or spectral-shift dimensions layered onto the present architecture; and dynamic, spatial-light-modulator-based generation of additional virtual triggers along the lines discussed in Section 2.2. A full three-trigger, 49-plane system – assembled and characterized as a complete unit, rather than through the paired physical/cloned-trigger comparison reported in Section 6 – is likewise reserved for future work.

8. Conclusion and Future Work

This article has described the addition of a polarizing beam-splitter-cube layer to an existing eight-channel, non-polarized holographic trigger architecture, doubling it into 16 polarization-addressable channels through separation of each branch's light into orthogonal S and P components. Two encoder stages, each a direct reproduction of the base architecture's own encoder offset by the 90° separation between S and P, assign each of the 16 channels its own polarization angle. A fixed representational convention then maps the S-branch and P-branch channels to the positive and negative depth planes of a 49-plane display, with a 49th, polychromatic RGB reference channel drawn from a separate, ordinary trigger.

Future work includes assembling and characterizing the complete three-trigger, 49-plane system as a single unit, and extending the polarization-cloning principle to other orthogonal-polarization pairs and other polarizing-prism types. It also includes combining the present cloning mechanism with additional physical multiplexing dimensions – zoom-state, global-convergence-angle, and spectral-shift multiplication – and exploring a spatial-light-modulator-based, dynamically reconfigurable realization of the recorded zoom teletransfer system described in Section 4.

References

[1]. J. An, K. Won, Y. Kim, J.-Y. Hong, et al., Slim panel holographic video display, *Nature Communications*, Vol. 11, 2020, 5568.

[2]. A. Lagrange, A. Gilles, K. Heggarty, B. Fracasso, et al., Real-time calculation of Fresnel holograms using the split-Lohmann method, *Optics Letters*, Vol. 50, Issue 8, 2025, pp. 2554-2557.

[3]. T. Wu, J. Ma, C. Wang, H. Wang, et al., Full-color see-through three-dimensional display method based on volume holography, *Sensors*, Vol. 21, Issue 8, 2021, 2698.

[4]. G. Ivanova, B. Ivanov, D. Dimov, A 24-channel optical trigger for use in 3D holographic display systems, in *Proceedings of the 9th International Conference on Optics, Photonics and Lasers (OPAL)*, 2026, pp. 35-39.

[5]. B. Ivanov, G. Ivanova, D. Dimov, Design and fabrication of a 24-channel holographic optical trigger for high-speed optical computation, in *Proceedings of the 9th International Conference on Optics, Photonics and Lasers (OPAL)*, 2026, pp. 86-91.

[6]. S. J. Zheng, J. R. Tan, H. J. Liu, X. Lin, et al., Orthogonal matrix of polarization combinations: Concept and application to multichannel holographic recording, *Opto-Electronic Advances*, Vol. 7, 2024, 230180.

[7]. B. Ivanov, M. Shopova, A. Baldjiev, E. Stoykova, et al., Four-channel holographic infrared optical element, *Proceedings of SPIE*, Vol. 7747, 2011, 77470K.

[8]. X. Xu, Z. Lu, H. Pan, S. Zhou, et al., Polarization-encoded switchable structured light generator based on all-dielectric holographic metasurfaces, *Coatings*, Vol. 16, Issue 7, 2026, 858.

[9]. Q. Hou, S. Xu, Z. Li, C. Chi, et al., Full-color multi-depth holographic pancake display, *Optics Express*, Vol. 34, Issue 13, 2026, pp. 24805-24828.

[10]. Q. Han, T. Wang, G. Zhang, W. Kamal, et al., Holographic projection display enlargement via polarization grating beam steering with fast-response liquid crystal pi cells, *ACS Photonics*, Vol. 13, Issue 10, 2026, pp. 2943-2953.

[11]. J. Wang, J. Chen, F. Yu, R. Chen, et al., Unlocking ultra-high holographic information capacity through nonorthogonal polarization multiplexing, *Nature Communications*, Vol. 15, 2024, 6284.

[12]. Y. Liu, Y.-T. Xiao, X.-Y. Huo, Q. Cai, et al., Dynamic holographic display with multiplexed dielectric metasurfaces, *Nanophotonics*, Vol. 15, Issue 12, 2026, e70114.

[13]. Y. Ye, H. Su, Y. Jia, B. Li, et al., High-capacity multiview display with large viewing angle via orbital angular momentum encoded nanograting arrays, *Nanophotonics*, Vol. 14, Issue 24, 2025, pp. 4341-4350.

[14]. F. Shen, Z. Mao, W. Fan, J. Wu, et al., OAM multiplication operator enabled holographic multiplexing, *Light: Science & Applications*, Vol. 15, 2026, 18.

[15]. Q. Ji, H. Deng, H. Zhang, W. Jiang, et al., Optical see-through 2D/3D compatible display using variable focus lens and multiplexed holographic optical elements, *Photonics*, Vol. 8, Issue 8, 2021, 297.

[16]. A. Márquez, C. Li, A. Beléndez, S. A. Maier, et al., Information multiplexing from optical holography to multi-channel metaholography, *Nanophotonics*, Vol. 12, Issue 24, 2023, pp. 4415-4440.

[17]. H. Kogelnik, Coupled wave theory for thick hologram gratings, *Bell System Technical Journal*, Vol. 48, Issue 9, 1969, pp. 2909-2947.

[18]. D. Gabor, A new microscopic principle, *Nature*, Vol. 161, Issue 4098, 1948, pp. 777-778.

[19]. P. Hariharan, Optical Holography: Principles, Techniques and Applications (2nd ed.), *Cambridge University Press*, Cambridge, 1996.

[20]. F. Wang, J. Starobrat, Y. Wang, M. Goto, et al., Local zoom issue in holographic 3D display, *Journal of Physics: Photonics*, Vol. 8, Issue 3, 2026, 035019.

[21]. K. H. Kwon, M.-U. Erdenebat, N. Kim, A. Khuderchuluun, et al., High-quality 3D visualization system for light field microscopy with fine-scale shape measurement through accurate 3D surface data, *Sensors*, Vol. 23, Issue 4, 2023, 2173.

[22]. Y. Ning, S. Chen, D. Gao, Y. Zhou, et al., Deformation strategy of deformable mirrors for a typical zooming system, *Applied Optics*, Vol. 63, Issue 8, 2024, pp. 2311-2320.

[23]. P. Gentet, Y. Gentet, S.-H. Lee, Ultimate 04: The new reference for ultra-realistic color holography, in *Proceedings of the International Conference on Emerging Trends & Innovation in ICT (ICEI)*, 2017, pp. 162-166.

[24]. B. Ivanov, M. Shopova, E. Stoykova, V. Sainov, Reconstruction of silver halide volume reflection holograms at the wavelengths of recording, *Optica Applicata*, Vol. 42, Issue 3, 2012, pp. 643-650.

[25]. D. De Ceglia, A. Alù, D. N. Neshev, C. De Angelis, Analog image processing with nonlinear nonlocal flat optics, *Optical Materials Express*, Vol. 14, Issue 1, 2024, pp. 92-100.

[26]. U. Gudelek, E. Sahin, A. Gotchev, Perceptually optimized model for near eye light field reconstruction, in *Proceedings of the IEEE International Workshop on Multimedia Signal Processing (MMSP)*, 2023, pp. 1-6.

[27]. LETO-3 phase only spatial light modulator datasheet, HOLOEYE Photonics AG, https://holoeye.com/products/spatial-light-modulators/leto-3-phase-only/

Published by International Frequency Sensor Association (IFSA) Publishing, S. L., 2026 (http://www.sensorsportal.com).